

# Padé Theory and Phenomenology of Resonance Poles

Juan José Sanz-Cillero <sup>1</sup>

*Grup de Física Teòrica and IFAE, Universitat Autònoma de Barcelona, E-08193 Bellaterra (Barcelona), Spain*

---

## Abstract

The use of Padé approximants for the description of QCD matrix elements is discussed in this talk. We will see how they prove to be an extremely useful tool, specially in the case of resonant amplitudes. It will allow the inclusion of high-energy Euclidian data to improve the determination of low-energy properties, such as the quadratic vector radius. This does not mean that the rational approximations can be arbitrarily employed for the extraction of any desired hadronic parameter. A discussion about the validity, limitations and possible issues of the Padé analysis is carried on along the paper. Finally, based on the de Montessus de Ballore's theorem, a theoretically safe new procedure for the extraction of the pole mass and width of resonances is proposed here and illustrated with the example of the  $\rho(770)$ .

*Keywords:*

Padé Approximation, Hadronic poles and properties

*PACS:* 11.55.Bq, 12.40.Vv, 12.40.Yx, 14.40.Be,

*2010 MSC:* 41A21

---

## 1. Introduction

Quantum Chromodynamics (QCD) has been proven to be the right theory to describe the strong dynamics interactions. However, in the non-perturbative regime one finds resonant structures in the cross section which can be related with the presence of short-lived intermediate hadronic states, usually referred as resonances. From a mathematical point of view, these states appeared as complex poles of the amplitude in the transferred energy at higher complex Riemann sheets, other than the physical one. Typically, the amplitude grows abruptly when the energy gets close to the resonance pole, remaining nevertheless finite all the way as the singularity is located off the real axis, at a complex value of the energy.

One of the clearest examples of this kind of resonant amplitudes is the  $\pi\pi$ -vector form-factor (VFF). There, the spectral function is dominated by a very pronounced  $\rho(770)$  meson peak and essentially no other big effect is observed. Through this qualitative knowledge of the spectral function in the Minkowsky region ( $q^2 > 0$ ) and the experimental data from the Euclidean region ( $q^2 < 0$ ) one is able to extract properties of the VFF at the origin [1]. Its first and second derivatives were determined at  $q^2 = 0$  (respectively related to the quadratic vector radius  $\langle r^2 \rangle_V^\pi$  and the curvature  $c_V^\pi$ ) by means of Padé approximants (PA) centered at the origin [1]. However, this precise procedure does not allow us to make predictions for properties of the amplitude above threshold, such as the  $\rho$ -meson pole position.

Indeed, the potential danger of using rational approximants for the extraction of resonance pole positions is shown with the help of a model. Under some limits the PAs result equivalent to some unitarization procedures, such as the inverse amplitude method (IAM) [2, 3], reason why these unitarizations have been sometimes loosely called “Padés”. We performed a perturbative computation in the linear sigma model (LSM) and found that the PA around the origin led to improper determinations of the meson mass and width [4]. However, we will show here that by an adequate

---

<sup>1</sup>Proceedings of the *Conference on Approximation and Extrapolation of Convergent and Divergent Sequences and Series*, CIRM Luminy, Marseille (France), September 28th - October 2nd 2009. I would like to thank the organizers of the conference their invitation and the nice scientific and interdisciplinary environment. This work is supported in part by CICYT-FEDER-FPA2008-01430, SGR2009-894, the Spanish Consolider-Ingenio 2010 Program CPAN (CSD2007-00042), the Juan de la Cierva Program and the EU Contract No. MRTN-CT-2006-035482, FLAVIANet.

reinterpetation of the PA it is possible to converge (though slowly) to the actual low-energy constants (LEC) of the model. Nonetheless, the perturbative calculation only makes sense in the LSM when the  $\sigma - \pi\pi$  interaction is weak. It has been argued that the unitarization procedures such as IAM are expected to work for cases of strongly interacting mesons, such as the physical  $\sigma(600)$ , and it is not intended for weakly interacting theories [5]. This issue is still unclear and will require of further clarifications.

Still, the Padé approximants allow us to produce a model independent determination of the resonance poles if they are adequately employed. To do this in a theoretically safe way, we need to center our Padé above the branch-cut singularity (beyond the first production threshold), not below (at the origin). This modification also makes possible the direct use of Minkowsky data, being now the Euclidean ones discarded.

The importance of these hadronic pole parameters is that usually one relates an observable with the corresponding renormalized couplings but in the resonance case in QCD there is still plenty of debate about which is the right lagrangian formulation. Alternatively, the resonance pole positions in the complex energy plane are universal for all the processes with those same quantum numbers. They do not depend on a particular lagrangian realization. Nonetheless, in many cases extracting these hadronic properties brings along much model dependence as it is not clear how to extrapolate from the data on the real energy axis into the complex plane. This is highly non-trivial as one can see, for instance, observing the broad spreading of predictions for the  $\sigma(600)$  meson pole ( $I = J = 0$  channel in  $\pi\pi$ -scattering) [6].

The quadratic radius and curvature of the  $\pi\pi$ -VFF will be extracted in Sec. 2 with the help of Padés centered at  $q^2 = 0$ . A discussion on Padé unitarizations is provided in Sec. 3. Finally, a new kind of PA is proposed in Sec. 4 for the study of resonant amplitudes, centered at energies  $q^2$  over the first production threshold.

## 2. Padé approximants and the space-like VFF

Our goal in this section is the description of the  $\pi\pi$ -VFF  $F(Q^2)$  in the space-like region:

$$\langle \pi^+(p') | \frac{2}{3} \bar{u} \gamma^\mu u - \frac{1}{3} \bar{d} \gamma^\mu d - \frac{1}{3} \bar{s} \gamma^\mu s | \pi^+(p) \rangle = (p + p')^\mu F(Q^2), \quad (1)$$

where  $Q^2 = -q^2 = -(p' - p)^2$ , such that  $Q^2 > 0$  corresponds to space-like data. Since the spectral function for the corresponding dispersive integral for  $F(Q^2)$  starts at twice the pion mass, the form factor can be approximated by a Taylor expansion in powers of the momentum for  $|Q^2| < (2m_\pi)^2$ .

We want to construct an approximation that can be systematically improved upon. However, it will not be our aim to extract time-like properties from this analysis, like, for instance, vector meson mass predictions. It is neither our intention to describe the amplitude on the physical absorptive cut, above the  $\pi\pi$  threshold. Finally, it is convenient to remark that the results [1] presented here do not refer to any large- $N_C$  approximation but to the physical  $N_C = 3$  quantities.

### 2.1. The method: Padé approximants

Consider an analytical function  $F(z)$  at a point, e.g.,  $z = 0$ . A Padé approximant  $P_M^N(z) = Q_N(z)/R_M(z)$  is defined by the ratio of two polynomials of degrees  $N$  and  $M$  which agree with the original function  $F(z)$  up to the derivative of order  $N + M$  at  $z = 0$ :

$$P_M^N(z) - F(z) = O(z^{N+M+1}). \quad (2)$$

One may wonder what is new here with respect to a Taylor series of the form  $F(z) = a_0 + a_1 z + a_2 z^2 + \dots$ . The difference is that the polynomials are unable to go beyond the singular points. They are not able to describe them, setting those singularities the maximum size of the convergence disk (centered at the analytical point  $z = 0$ ). On the other hand, the poles of the PA tend to mimic the singular structure of the original function  $F(z)$ . For instance, if one studies the  $P_N^N(z)$  approximant of  $\ln(1 + z)$  all the poles are generated at the branch cut  $-\infty < z \leq -1$ , which gets more and more densely populated as  $N \rightarrow \infty$ .

Thus, in many cases, the PAs are found to work far beyond the analytical disk of convergence of the Taylor series. This allowed us to use space-like data to improve our description of the VFF at the analytical point  $Q^2 = 0$ . However, in general, the Padés converge over a compact region and, although this region may get larger and larger as one increases the order of the Padé, we did not use in this analysis information from the VFF at  $Q^2 = \infty$ .

It is convenient to remark that in the case of non-meromorphic functions, such as the physical amplitudes with logarithmic branch-cuts, the poles of the PA centered at the origin do not correspond to resonances, but rather to bumps and other structures in the spectral function over the logarithmic branch cut, which the PA tends to mimic.

In our phenomenological analysis of the VFF, we will use as inputs all the available data in the Euclidean region, which range from  $Q^2 = 0.01 \text{ GeV}^2$  up to  $10 \text{ GeV}^2$ . We will also make use of the qualitative knowledge we have on  $\pi\pi$ -VFF spectral function  $\rho(s)$ , essentially provided by the  $\rho(770)$  peak. This suggests the use of the  $P_1^L$  sequence for the description of this particular observable. The final aim of the analysis will be the extraction of the first and second derivatives at  $q^2 = 0$ , i.e., the quadratic vector radius  $\langle r^2 \rangle_V^\pi$  and the curvature  $c_V^\pi$ . From this perspective, the vector meson dominance expression  $F(Q^2) = (1 + Q^2/M^2)^{-1}$  is just a  $P_1^0$  Padé, the first term of a  $P_1^L$  sequence.

## 2.2. Theoretical uncertainties: playing with a phenomenological model

In order to illustrate the usefulness of the PAs as fitting functions, we will first use a phenomenological model as a theoretical laboratory to check our method. The model will also give us an idea about the size of possible systematic uncertainties.

We will consider a VFF phase-shift with the right threshold behavior and roughly the physical values of the rho mass and width. The form-factor is recovered through a once-subtracted Omnés relation,

$$F(Q^2) = \exp \left\{ -\frac{Q^2}{\pi} \int_{4\hat{m}_\pi^2}^{\infty} dt \frac{\delta(t)}{t(t+Q^2)} \right\}, \quad (3)$$

where  $\delta(t)$  plays the role of the vector form factor phase-shift [7, 8, 9] and is given by

$$\delta(t) = \tan^{-1} \left[ \frac{\hat{M}_\rho \hat{\Gamma}_\rho(t)}{\hat{M}_\rho^2 - t} \right], \quad (4)$$

with the  $t$ -dependent width given by

$$\hat{\Gamma}_\rho(t) = \Gamma_0 \left( \frac{t}{\hat{M}_\rho^2} \right) \frac{\sigma^3(t)}{\sigma^3(\hat{M}_\rho^2)} \theta(t - 4\hat{m}_\pi^2), \quad (5)$$

and  $\sigma(t) = \sqrt{1 - 4\hat{m}_\pi^2/t}$ . The input parameters are chosen to be close to their physical values:  $\Gamma_0 = 0.15 \text{ GeV}$ ,  $\hat{M}_\rho^2 = 0.6 \text{ GeV}^2$ ,  $4\hat{m}_\pi^2 = 0.1 \text{ GeV}^2$ . This model is actually quite realistic and it has been used for the extraction of the physical mass and width of the  $\rho(770)$  meson from time-like experimental data [7, 8, 9].

We generate now an emulation of the experimental data from our theoretical model. In order to recreate the situation of the experimental data [10]-[15] with the model, we have generated fifty “data” points in the region  $0.01 \leq Q^2 \leq 0.25$ , thirty data points in the interval  $0.25 \leq Q^2 \leq 3$ , and seven points for  $3 \leq Q^2 \leq 10$  (all these momenta in units of  $\text{GeV}^2$ ). These points are taken with vanishing error bars since our purpose here is to estimate the systematic error derived purely from our approximate description of the form factor.

These generated data is then fitted through  $P_1^L$  Padé approximants,

$$P_1^L(Q^2) = 1 + \sum_{k=0}^{L-1} a_k (-Q^2)^k + (-Q^2)^L \frac{a_L}{1 + \frac{a_{L+1}}{a_L} Q^2}, \quad (6)$$

where the vector current conservation condition  $P_1^L(0) = 1$ , i.e.,  $a_0 = 1$ , has been imposed. At low energies this produces for the Taylor coefficients  $a_j$  the prediction

$$F(Q^2) = 1 - a_1 Q^2 + a_2 Q^4 - a_3 Q^6 + \dots \quad (7)$$

This leads to a series of predictions for the low-energy parameters, which are compared to their (known) exact values in Table 1. The last PA we have fitted to these data is  $P_1^6$ . Notice that the pole position of the Padés differs from the mass parameter of the model  $\hat{M}_\rho^2$ —and this from the pole mass—. This example makes explicit how one can get a

	$P_1^0$	$P_1^1$	$P_1^2$	$P_1^3$	$P_1^4$	$P_1^5$	$P_1^6$	$F(Q^2)(\text{exact})$
$a_1(\text{GeV}^{-2})$	1.549	1.615	1.639	1.651	1.660	1.665	1.670	1.685
$a_2(\text{GeV}^{-4})$	2.399	2.679	2.809	2.892	2.967	3.020	3.074	3.331
$a_3(\text{GeV}^{-6})$	3.717	4.444	4.823	5.097	5.368	5.579	5.817	7.898
$s_p(\text{GeV}^2)$	0.646	0.603	0.582	0.567	0.552	0.540	0.526	$\hat{M}_\rho^2 = 0.6$

Table 1: Results of the various fits to the form factor  $F(Q^2)$  in the model, Eq. (3). The exact values for the coefficients  $a_i$  in Eq. (7) are given on the last column. The last row shows the predictions for the corresponding pole for each Padé ( $s_p$ ), to be compared to the mass parameter  $\hat{M}_\rho^2 = 0.6 \text{ GeV}^2$  in the model.

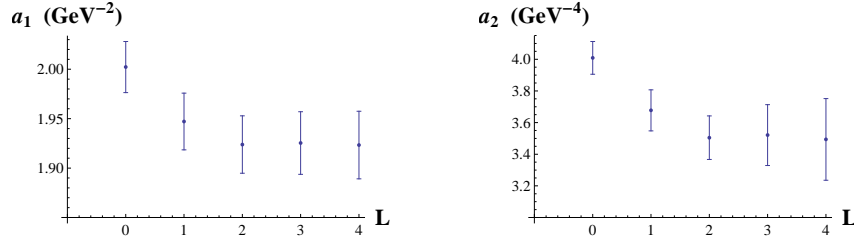


Figure 1: Value of the  $a_1$  and  $a_2$  Taylor coefficients for the  $P_1^L$  sequence of Padé Approximants obtained from experimental data fits [10]–[15].

rather precise value for the Taylor coefficients in Eq. (7) without an accurate knowledge of the spectral function (i.e., of the time-like region).

Based on the previous results, we will take the values in Table 1 as a rough estimate of the systematic uncertainties when fitting to the experimental data in the following sections. Since, as we will see, the best fit to the experimental data comes from the Padé  $P_1^4$ , we will take the error in Table 1 from this Padé as a reasonable estimate and, respectively, add to the final error an extra systematic uncertainty of 1.5% and 10% for  $a_1$  and  $a_2$ .

### 2.3. Experimental pion vector form factor

The prominent role of the rho meson contribution motivates the use of the  $P_1^L$  Padé sequence as the central tool for the study of this amplitude, later complemented by other types of Padés. The fit of  $P_1^L$  to the space-like data points in Refs. [10]–[15] determines the coefficients  $a_k$  that best interpolate them. Fig. 1 shows the evolution of the fit results for the Taylor coefficients  $a_1$  and  $a_2$  for the  $P_1^L$  PA from  $L = 0$  up to  $L = 4$ . As one can see, after a few Padés these coefficients become stable. For the data in Refs. [10]–[15], this happened at  $L = 4$ . The  $P_1^4$  Padé Approximant provides our best fit and, upon expansion around  $Q^2 = 0$ , this yields

$$a_1 = 1.92 \pm 0.03 \text{ GeV}^{-2}, \quad a_2 = 3.49 \pm 0.26 \text{ GeV}^{-4}; \quad (8)$$

with a  $\chi^2/\text{dof} = 117/90$  [1].

Eq. (6) shows that the pole of each  $P_1^L$  PA is determined by the ratio  $s_p = a_L/a_{L+1}$ . This ratio is shown in Fig. 2, together with a gray band given by  $M_\rho^2 \pm M_\rho \Gamma_\rho$  for comparison. From this figure one can see that the position of the pole of the PA is close to the physical mass  $M_\rho^2$  [6], although it cannot be identified with it, as we already saw in the model of the previous subsection. The  $P_1^L$  pole  $s_p$  is always real and lies at the “bump” of the spectral fraction, in the range  $M_\rho^2 \pm M_\rho \Gamma_\rho$ . The Padé tends to reproduce the  $\rho$  peak line-shape but, obviously, no complex resonance pole can be recovered from a  $P_1^L$  Padé at higher Riemann sheets.

As one can see in Fig. 3, the sequence  $P_1^L$  converges to the physical form-factor in the data region but, eventually, it diverges like  $(Q^2)^{L-1}$ . These PAs only converge on a compact region of the complex plane and are unable to recover the  $1/Q^2$  asymptotic behaviour prescribed by QCD at short distances [16]. Nonetheless, the important fact is that the Padés allow the use of data not only by the origin but even from energies as large as  $Q^2 \sim 10 \text{ GeV}^2$ , something that a normal Taylor expansion at the origin does not permit.

This  $P_1^L$  PA analysis was complemented with the results from other types of Padés: two-pole Padé approximants  $PA_2^L$ ; one, two and three-pole Padé-types (PT) with the poles fixed beforehand; two-pole partial Padés  $PP_{1,1}^L$ , with one

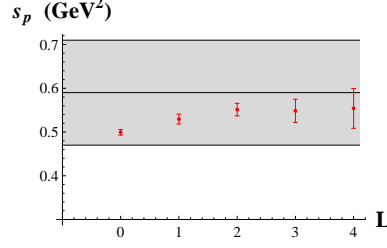


Figure 2: Position  $s_p$  of the pole for the different  $P_1^L$ . The range with the physical values  $M_\rho^2 \pm M_\rho \Gamma_\rho$  is shown (gray band) for comparison.

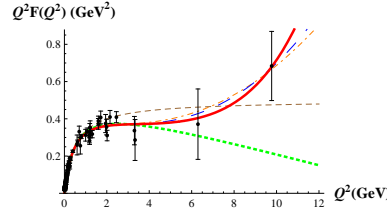


Figure 3: The sequence of  $P_1^L$  PAs is compared to the available space-like data [10]-[15]:  $P_1^0$  (brown dashed),  $P_1^1$  (green thick-dashed),  $P_1^2$  (orange dot-dashed),  $P_1^3$  (blue long-dashed),  $P_1^4$  (red solid).

	$PA_2^L$	$PT_1^L(\rho)$	$PT_2^L(\rho, \rho')$	$PT_2^L(\rho, \rho'')$	$PT_3^L(\rho, \rho', \rho'')$	$PP_{1,1}^L(\rho)$
$a_1(\text{GeV}^{-2})$	$1.924 \pm 0.029$	$1.90 \pm 0.03$	$1.902 \pm 0.024$	$1.899 \pm 0.023$	$1.904 \pm 0.023$	$1.902 \pm 0.029$
$a_2(\text{GeV}^{-4})$	$3.50 \pm 0.14$	$3.28 \pm 0.09$	$3.29 \pm 0.07$	$3.27 \pm 0.06$	$3.29 \pm 0.09$	$3.28 \pm 0.09$

Table 2: Different results for two-pole Padé approximants, Padé-types and partial Padés, where we used the  $\rho$ ,  $\rho'$ , and  $\rho''$  masses.

pole fixed beforehand and the other determined by the low-energy coefficients  $a_k$ . The different results are gathered in Table. 2.

Combining all the previous rational approximants results in the average given by [1]

$$a_1 = 1.907 \pm 0.010_{\text{stat}} \pm 0.03_{\text{syst}} \text{ GeV}^{-2}, \quad a_2 = 3.30 \pm 0.03_{\text{stat}} \pm 0.33_{\text{syst}} \text{ GeV}^{-4}. \quad (9)$$

The first error comes from combining the results from the different fits by means of a weighted average. On top of that, we have added what we believe to be a conservative estimate of the theoretical (i.e. systematic) error based on the analysis of the VFF model in the previous subsection. We expect the latter to give an estimate for the systematic uncertainty due to the approximation of the physical form factor with rational functions. For comparison with previous

	$\langle r^2 \rangle_V^\pi (\text{fm}^2)$	$a_2 (\text{GeV}^{-4})$
This work	$0.445 \pm 0.002_{\text{stat}} \pm 0.007_{\text{syst}}$	$3.30 \pm 0.03_{\text{stat}} \pm 0.33_{\text{syst}}$
PDG [6]	$0.452 \pm 0.011$	...
CGL [17, 18]	$0.435 \pm 0.005$	...
TY [19]	$0.432 \pm 0.001$	$3.84 \pm 0.02$
BCT [20]	$0.437 \pm 0.016$	$3.85 \pm 0.60$
PP [9]	$0.430 \pm 0.012$	$3.79 \pm 0.04$
Lattice [21]	$0.418 \pm 0.031$	...

Table 3: Our results for the quadratic vector radius  $\langle r^2 \rangle_V^\pi$  and second derivative  $a_2$  are compared to other determinations [6, 9, 17, 18, 19, 20, 21]. Our first error is statistical. The second one is systematic, based on a previous analysis of a VFF model.

analyses, we also provide in Table 3 the value of the quadratic vector radius, which is given by  $\langle r^2 \rangle_V^\pi = 6 a_1$ .

In summary, we used rational approximants as a tool for fitting the pion vector form factor in the Euclidian range. Since these approximants are capable of describing the region of large momentum, we think they are better suited than polynomials for the description of the currently available space-like data. As our results in Table 2 show, the errors achieved with these approximants are competitive with previous analyses existing in the literature, based on more elaborated techniques.

### 3. A critical look on Padé unitarizations

Exact unitarity is an important additional piece of information that eventually needs to be included in the description of the scattering processes. A commonly employed unitarization procedure is the inverse amplitude method (IAM) [2, 3, 22, 23, 24]. Although it can be formulated in a more elaborated way through dispersion relations, the method relies in the unitarity relation in the elastic region, which in the massless case has the simplified form,

$$\text{Im}t(s) = |t(s)|^2 \quad \longrightarrow \quad \text{Im}[t(s)^{-1}] = -1. \quad (10)$$

This fixes completely the imaginary part of the inverse partial-wave amplitude  $t(s)^{-1}$  on the elastic part of the right-hand cut ( $s > 0$ ). All that remains in  $t(s)^{-1} = \text{Re}[t(s)^{-1}] + \text{Im}[t(s)^{-1}]$  is to determine the real part of  $t(s)^{-1}$ , which is fixed in the IAM through a low-energy matching to  $\chi$ PT:

$$t(s)_{\chi PT} = t_{(2)} + t_{(4)} + t_{(6)} + \dots \quad (11)$$

where the  $t_{(k)}$  are the contributions corresponding to  $O(p^k)$  in  $\chi$ PT. Hence, depending on the order of the matching one obtains a sequence of unitarized amplitudes [2, 3, 22, 23, 24]:

$$O(p^4) \longrightarrow t_{IAM} = \frac{t_{(2)}}{1 - t_{(4)}/t_{(2)}}, \quad O(p^6) \longrightarrow t_{IAM} = \frac{t_{(2)}}{1 - t_{(4)}/t_{(2)} - t_{(6)}/t_{(2)} + (t_{(4)}/t_{(2)})^2}, \quad \dots \quad (12)$$

Identical results are obtained if one recovers the partial wave amplitude through a dispersion relation and matches  $\chi$ PT on the left-hand cut.

In the tree-level limit, the IAM expressions (12) become a series of Padé approximants of the form  $P_1^1$ ,  $P_2^1$ , etc, reason why these unitarizations are sometimes called “Padés”. In any case, it is in this limit that one can use all the powerful technology of the mathematical theory of Padé approximants. However, it has been argued that the IAM should be only applicable for the description of broad resonances, such as the sigma meson, and not narrow states [5].

The IAM has been found to described the data reasonably well even, in some cases, up to energies as high as  $\sqrt{s} \sim 1$  GeV [2, 3]. It has been able to generate all the resonances below 1 GeV:  $\rho$ ,  $K^*$ ,  $\sigma$  (or  $f_0(600)$ ),  $\kappa$ ,  $a_0(980)$  and  $f_0(980)$  [2, 3, 23, 24], and the expected  $N_C$  behaviour of the  $\rho$  and  $K^*$  poles as  $q\bar{q}$  states has been recovered [23].

However, one may wonder what information is lost when  $\text{Re}[t(s)^{-1}]$  is fixed at low energies with  $\chi$ PT. Likewise, in general the unitarized amplitudes violate crossing, as only it only resums a particular set of diagrams in the  $s$ -channel, not in the crossed ones. Nevertheless, even though the IAM determinations have produces good numerical results, this is not supported by the theory of Padé approximants. Thus, we consider that the theoretical reason why the IAM has been so successful at the phenomenological level still needs and deserves further clarifications.

#### 3.1. A counterexample: The $\sigma$ in the Linear Sigma Model

The application of the IAM to the linear sigma model (LSM) was proposed in Ref. [4] as a counterexample, to show how the prediction from unitarizing the low-energy LSM led to very different pole mass and width than those actually in the LSM.

At tree-level, the sigma mass is found to be  $M_\sigma^2 = 2\mu^2$ , and the width is zero. At next-to-leading order, the sigma pole gets shifted due to the quartic potential, i.e.,  $M_\sigma^2 = 2\mu^2 + O(g)$ , and the width becomes different from zero. For simplicity, the massless pion limit is assumed.

In order to determine the scalar meson mass and width up to  $O(g)$ , we compute the one-loop sigma correlator [25],

$$i\Delta(s)^{-1} = s - M_\sigma^2 \left[ 1 + \frac{3g}{16\pi^2} \left( -\frac{13}{3} + \ln \frac{-s}{M_\sigma^2} + 3\rho(s) \ln \left( \frac{\rho(s) + 1}{\rho(s) - 1} \right) \right) + O(g^2) \right], \quad (13)$$

where  $\rho(s) \equiv \sqrt{1 - 4M_\sigma^2/s}$  and the term  $-13/3$  is determined by the renormalization scheme chosen by Ref. [25], which sets the relation  $2gF^2 = M_\sigma^2$  at the one-loop order, with  $F$  the pion decay constant and  $M_\sigma$  the renormalized mass parameter. Now it is possible to extract the pole  $s_p$  of the propagator up to the considered order in perturbation theory. If one approaches the branch cut from the upper part of the complex  $s$ -plane, the pole in the second Riemann sheet is located at  $s_p = (M_p - i\Gamma_p/2)^2$ , with the pole mass and width,

$$\begin{aligned} \left( \frac{M_p^2}{M_\sigma^2} \right)_{LSM} &= 1 + \frac{3g}{16\pi^2} \left( -\frac{13}{3} + \pi\sqrt{3} \right) + \mathcal{O}(g^2) \\ \left( \frac{M_p \Gamma_p}{M_\sigma^2} \right)_{LSM} &= \frac{3g}{16\pi} + \mathcal{O}(g^2). \end{aligned} \quad (14)$$

The  $\pi\pi$ -scattering is determined by the  $\pi^+\pi^- \rightarrow \pi^0\pi^0$  amplitude  $A(s, t, u)$ . This defines the isospin amplitudes

$$\begin{aligned} T(s, t, u)^{I=0} &= 3A(s, t, u) + A(t, s, u) + A(u, t, s), \\ T(s, t, u)^{I=1} &= A(t, s, u) - A(u, t, s), \\ T(s, t, u)^{I=2} &= A(t, s, u) + A(u, t, s), \end{aligned} \quad (15)$$

and the partial wave projection provided by

$$t_J^I(s) = \frac{1}{64\pi} \int_{-1}^1 d\cos\theta P_J(\cos\theta) T(s, t, u)^I, \quad (16)$$

where  $\theta$  is the scattering angle in the  $\pi\pi$  center-of-mass rest frame.

We now consider the LSM at low energies, which reproduces the structure prescribed by  $\chi$ PT. Hence, for the first partial waves  $t_J^I(s)$ , with  $IJ = 00, 11, 20$ , it produces the  $\mathcal{O}(p^2)$  amplitudes,

$$t_0^0(s)_{(2)} = \frac{s}{16\pi F^2}, \quad t_1^1(s)_{(2)} = \frac{s}{96\pi F^2}, \quad t_0^2(s)_{(2)} = -\frac{s}{32\pi F^2}, \quad (17)$$

and at  $\mathcal{O}(p^4)$ ,

$$\begin{aligned} t_0^0(s)_{(4)} &= t_0^0(s)_{(2)} \times \frac{11s}{6M_\sigma^2} \left[ 1 - \frac{g}{264\pi^2} \left( 18 \ln \frac{-s}{M_\sigma^2} + 7 \ln \frac{s}{M_\sigma^2} + \frac{193}{3} \right) + \mathcal{O}(g^2) \right], \\ t_1^1(s)_{(4)} &= t_1^1(s)_{(2)} \times \left( \frac{-s}{M_\sigma^2} \right) \left[ 1 + \frac{g}{48\pi^2} \left( \ln \frac{-s}{M_\sigma^2} - \ln \frac{s}{M_\sigma^2} - \frac{26}{3} \right) + \mathcal{O}(g^2) \right], \\ t_0^2(s)_{(4)} &= t_0^2(s)_{(2)} \times \left( \frac{-2s}{3M_\sigma^2} \right) \left[ 1 - \frac{g}{24\pi^2} \left( \frac{9}{4} \ln \frac{-s}{M_\sigma^2} + \frac{11}{4} \ln \frac{s}{M_\sigma^2} + \frac{163}{24} \right) + \mathcal{O}(g^2) \right]. \end{aligned} \quad (18)$$

The Inverse Amplitude Method (IAM) provides an amplitude that is unitary not only at the perturbative level but exactly. At  $\mathcal{O}(p^4)$ , one has the unitarized amplitude,  $t_{IAM} = \frac{t_{(2)}}{1 - \frac{t_{(4)}}{t_{(2)}}}$ , which has its poles  $s_p$  at  $t_{(2)}(s_p) = t_{(4)}(s_p)$ :

$$\mathbf{IJ=00} \longrightarrow s_p = \frac{6}{11} M_\sigma^2 \left[ 1 + \frac{g}{264\pi^2} \left( \frac{193}{3} + 25 \ln \frac{6}{11} - 18i\pi \right) + \mathcal{O}(g^2) \right], \quad (19)$$

$$\mathbf{IJ=11} \longrightarrow s_p = -M_\sigma^2 \left[ 1 + \frac{g}{48\pi^2} \left( \frac{26}{3} + i\pi \right) + \mathcal{O}(g^2) \right], \quad (20)$$

$$\mathbf{IJ=20} \longrightarrow s_p = -\frac{3}{2} M_\sigma^2 \left[ 1 + \frac{g}{24\pi^2} \left( \frac{163}{24} + 5 \ln \frac{3}{2} + \frac{11i\pi}{4} \right) + \mathcal{O}(g^2) \right]. \quad (21)$$

These are the poles that appear in the unphysical Riemann sheet as one approaches from upper half of the first Riemann sheet. There is also a conjugate pole at  $s_p^*$  if one approaches the real  $s$ -axis from below.

The first thing to be noticed is that poles appear in the  $IJ = 11$  and 20 channels even for small values of  $g$ , contrary to what one expects in the LSM, where no meson with these quantum numbers exists. Furthermore, these “states” are not resonances, as they are located on the left-hand side of the complex  $s$ -plane, out of the physical Riemann sheet, and carrying a negative squared mass.

One can easily see the important disagreement between the actual LSM value for the pole mass and width given in Eq. (14) and the posterior IAM “prediction”,

$$\begin{aligned} \left( \frac{M_p^2}{M_\sigma^2} \right)_{IAM} &= \frac{6}{11} \left[ 1 + \frac{g}{16\pi^2} \left( \frac{50}{33} \ln \frac{6}{11} + \frac{386}{99} \right) + \mathcal{O}(g^2) \right], \\ \left( \frac{M_p \Gamma_p}{M_\sigma^2} \right)_{IAM} &= \frac{24}{121} \cdot \frac{3g}{16\pi} + \mathcal{O}(g^2), \end{aligned} \quad (22)$$

this is,  $(M_p^2)_{IAM} \simeq 50\% (M_p^2)_{LSM}$  and  $(M_p \Gamma_p)_{IAM} \simeq 20\% (M_p \Gamma_p)_{LSM}$ .

### 3.2. Higher order Padé Approximants for the LSM

In the tree-level limit (for instance, at large  $N_C$ ), the IAM amplitudes become Padé approximants centered at  $s = 0$ :

$$\begin{aligned} [O(p^4)] \quad \frac{t_{(2)}}{1 - t_{(4)}/t_{(2)}} &= t_{(2)} + t_{(4)} + \dots \longrightarrow P_1^1(s) \\ [O(p^6)] \quad \frac{t_{(2)}}{1 - t_{(4)}/t_{(2)} - t_{(6)}/t_{(2)} + (t_{(4)}/t_{(2)})^2} &= t_{(2)} + t_{(4)} + t_{(6)} + \dots \longrightarrow P_2^1(s) \\ &\dots \end{aligned}$$

The  $\pi\pi$ -scattering is given in the LSM case by

$$A(s, t, u) = \frac{s}{F^2} \frac{M_\sigma^2}{M_\sigma^2 - s} \longrightarrow t_0^0(s) = \frac{M_\sigma^2}{32\pi F^2} \left[ -5 + \frac{3M_\sigma^2}{M_\sigma^2 - s} + \frac{2M_\sigma^2}{s} \ln \left( 1 + \frac{s}{M_\sigma^2} \right) \right], \quad (23)$$

which at low energies become,

$$A(s, t, u) = \frac{s}{F^2} \left[ 1 + \frac{s}{M_\sigma^2} + \frac{s^2}{M_\sigma^4} + \dots \right] \longrightarrow t_0^0(s) = \frac{s}{16\pi F^2} \left[ 1 + \frac{11s}{6M_\sigma^2} + \frac{15s^2}{12M_\sigma^4} + \dots \right]. \quad (24)$$

The first Padé approximant,  $P_1^1$ , gives for the  $\sigma$  pole the prediction  $s_p = \frac{6}{11} M_\sigma^2$ . But how does the series  $P_1^1, P_2^1, P_3^1, \dots$  evolve? One could even wonder, for instance, about the behaviour of other sequences such as  $P_1^1, P_2^2, P_3^3, \dots$ . We have shown in Fig. 4 the  $P_M^1$  sequence up to such a high order as  $P_{61}^1$ . One can see the extremely slow converges, with the pole prediction still a 30% off for  $P_{61}^1$ . Furthermore, this kind of  $P_M^1$  Padé approximants has only one zero (at  $s = 0$ ) and places the  $M$  poles in a circle centered at  $s = 0$ , producing an analytical structure completely different to that in the actual LSM.

On the other hand, a quick convergence is found for the diagonal Padé sequence  $P_N^N$ :  $P_1^1$  reproduces the sigma pole a 40% off but  $P_2^2$  disagrees by less than 1%,  $P_3^3$  by less than 0.1%, etc. Likewise, Fig. 5.b shows how the  $P_N^N$  sequence, besides providing the isolated pole of the sigma, tends to reproduce the left-hand cut as  $N$  increases. The poles of  $P_{20}^{20}$  are plotted there. Although a PA is a rational function without cuts, these are mimicked by placing poles where the cuts should lie. The  $P_{20}^{20}$  has one isolated pole near  $M_\sigma^2$  (with an accuracy of  $10^{-30}$ ) and nineteen poles over the real axis at  $s_p < -M_\sigma^2$ , i.e. on the left-hand cut of the original function. As  $N$  is increased, the number of poles lying on the branch cut increases too. A last remarkable feature is that the  $P_N^N$  approximants obey exact unitarity, as it happened with the IAM sequence  $P_N^1$ .

However, phenomenologically, the IAM has been usually employed for the study of the experimental data in the resonance region. These have been used to fit its parameters (e.g., the  $\hat{\ell}_i$  in Ref. [3]) and to extract the resonance pole positions. These parameters also provide a prediction for the chiral low-energy constants. However, although in general the convergence of these parameters to the LECs is unclear, in the case of the sequence of one-pole Padés  $P_1^N$



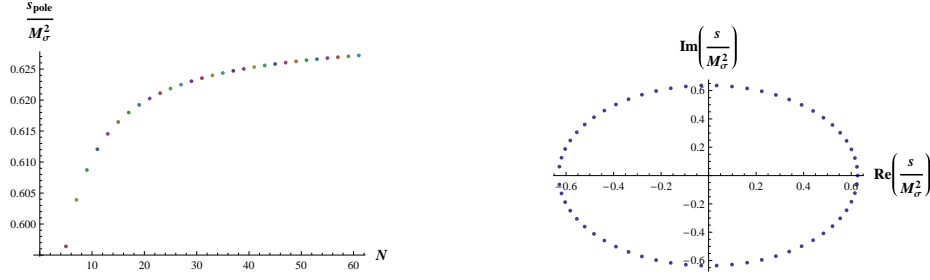


Figure 4: (a) Position of the nearest pole to  $M_\sigma^2$  for the first PAs of the form  $P_N^1$  with  $N$  odd (for even  $N$  all the poles are complex). (b) Poles of the  $P_{61}^1$  in the complex plane.

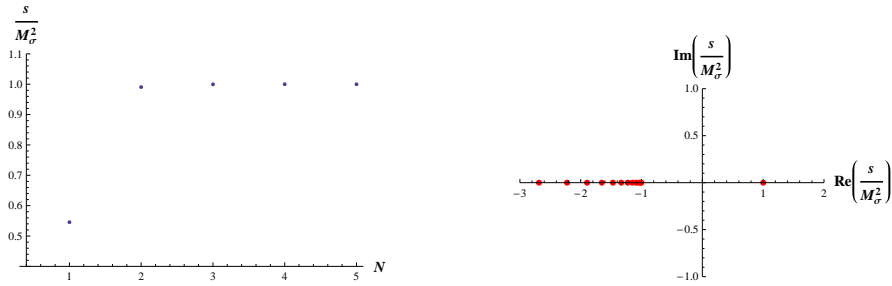


Figure 5: (a) Location of the closest pole to  $M_\sigma^2$  for the first  $P_N^N$  Padé approximants. (b) Poles of  $P_{20}^{20}$ .

centered at  $s \sim M_\sigma^2$ , the convergence is ensured in the disk centered at that point and with maximal radius limited by the position of the essential singularity of the left-hand cut at  $s = -M_\sigma^2$  [26, 27]. Hence, the predictions of the  $P_1^N$  Padé approximant at the middle point  $s = 0$  converge to the actual  $\chi$ PT low-energy couplings: the  $P_1^1$  centered at  $s = M_\sigma^2$  recovers the  $\mathcal{O}(p^4)$  coefficient with a 50% error, 31% for  $P_1^2$ , 17% for  $P_1^3$ , etc. From this perspective, maybe one could explain the phenomenological success of the IAM (which shares the first term,  $P_1^1$ ), although the  $P_1^N$  sequence might be more adequate for low-energy predictions than the usual IAM pattern  $P_N^1$ .

#### 4. Model independent determination of the resonance poles

As we have seen in previous sections, the Padés have been used to extract low-energy parameters from Euclidean data. In a misleading way, some unitarizations procedures have been called Padés, although their justification from the point of view of Padé theory is unclear. Though these unitarizations have been proven more or less successful in their predictions of the resonance poles and low-energy coefficients, they are not supported by the mathematical theory of Padés. Alternatively, in this section we show how it is possible to construct a different type of Padé approximants which allows us to use Minkowskian data and to extract the resonance pole position through a theoretically safe procedure supported by mathematical theorems.

To illustrate the procedure, let us start by the simplest possible case. If one has a function  $F(s)$  analytical in a disk  $B_\delta(s_0)$  then the Taylor series  $S_N(s) = \sum_{k=0}^N a_k(s - s_0)^k$  converges to  $F(s)$  in  $B_\delta(s_0)$  for  $N \rightarrow \infty$ , with the derivatives  $a_k = F^{(k)}(s_0)/k!$ . Experimentally, one usually does not have the derivatives at some point,  $s = s_0$ , but a series of experimental points  $F_j$  at different  $s_j$ , from which one extracts the function and its derivatives through polynomial fits with  $S_N(s)$  at higher and higher order  $N$ .

But, what happens if there is a single pole at  $s = s_p$  within the disk and  $F(s)$  is analytical everywhere else in  $B_\delta(s_0)$ ? In that case, the Taylor series does not converge any more. Nonetheless, the needed modification is not really big. In its simplest version with just one pole, the de Montessus de Ballore's theorem [26, 27] states that the sequence of one-pole Padé approximants  $P_1^N$  around  $s_0$  converges to  $F(s)$  in any compact subset of the disk excluding

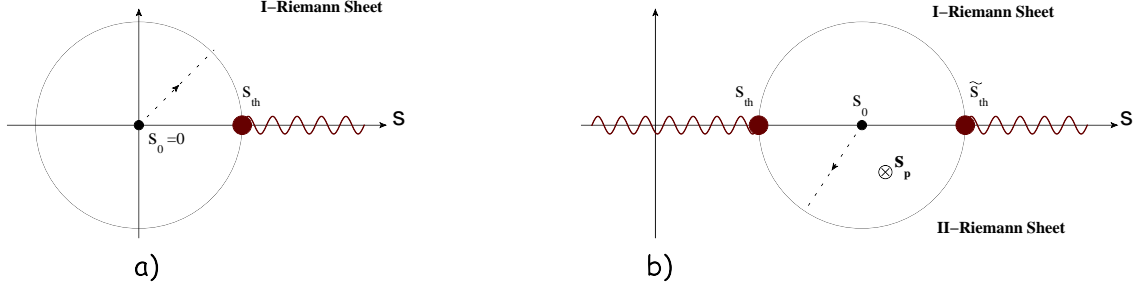


Figure 6: a) Analytical structure of the VFF below the first production threshold. b) Structure and analytical extension of the 1<sup>st</sup> Riemann sheet between the first and second production thresholds, with a resonance pole  $s_p$  in the 2<sup>nd</sup> Riemann sheet in the proximity of  $s_0$ .

the pole  $s_p$ :

$$P_1^N(s; s_0) = \sum_{k=0}^{N-1} a_k (s - s_0)^k + \frac{a_N (s - s_0)^N}{1 - \frac{a_{N+1}}{a_N} (s - s_0)}. \quad (25)$$

Hence, one finds that the Padé pole  $x_p = s_0 + \frac{a_N}{a_{N+1}}$  converges to  $s_p$  for  $N \rightarrow \infty$ . Experimentally, as referred before, one is not provided with the derivatives  $F(s_0)$ ,  $F'(s_0)$ ... but with the values  $F_j$  at different  $s_j$ . We use then the rational functions  $P_1^N$  as fitting functions (in the way done before with the polynomials). As  $N$  grows  $P_1^N$  gives an estimate of the series of derivatives  $\{F^{(k)}(s_0)\}$  and, hence, of the pole position  $s_p$ .

Usually, the Padés have been constructed around the low-energy point  $s_0 = 0$  (with  $s$ , typically the total square momentum). In matrix elements  $F(s)$  without left-hand cut, the amplitude is analytical from  $s = -\infty$  up to the first production threshold  $s_{th}$  and within the disk  $B_{s_{th}}(0)$  (see Fig. 6.a). For instance, one has  $s_{th} = 4m_\pi^2$  in the  $\pi\pi$  vector form-factor case. Experimentally, one may then have Euclidean data  $F^{\text{exp}}(s)$  at  $s < 0$  and use them to extract the derivatives of the VFF at  $s = 0$  [1]. Likewise, one may have Minkowskian data  $F^{\text{exp}}(s + i0^+)$  from  $s > s_{th}$  which, strictly, cannot be used by Padés centered at  $s_0 = 0$  due to the essential singularity at  $s = s_{th}$ .

Alternatively one can use in a theoretically safe way Padés centered at  $s_0 + i0^+$  over the brunch cut between the first and second production thresholds, with  $s_{th} < s_0 < \tilde{s}_{th}$  (see Fig. 6.b). In the  $\pi\pi$ -VFF this would correspond to the range between  $s_{th} = 4m_\pi^2$  and  $\tilde{s}_{th} = 4m_K^2$ , if multipion channels are neglected. One has then an analytical extension of our amplitude  $F(s)$  in the 1<sup>st</sup> Riemann sheet at  $s + i0^+$  into the 2<sup>nd</sup> Riemann sheet. Notice that the function  $F(s_0 + i0^+)$  and the derivatives in the  $a_k$  parameters are now complex numbers.

In the case of resonant amplitudes, a single pole appears in the second Reimann sheet in the neighbourhood of the real  $s$  axis, which can be related to the existence of a hadronic state –resonance– with the quantum numbers of that channel. One can use then the de Montessus de Ballore’s theorem [26, 27] for the description of the data in the maximal disk shown in Fig. 6.b. If the resonance pole lies within the disk the  $P_1^N$  Padé approximants allow its determination in a model independent way.

#### 4.1. Testing the method through various models

We consider a series of  $\rho$ -like models of the  $\pi\pi$  vector form-factor, with a single pole in the second Riemann sheet at  $s_p = (0.77 - \frac{i}{2}0.15)^2 \text{ GeV}^2$  and a logarithmic branch cut (starting at  $s = 0$  for sake of simplicity). The considered models were

$$\begin{aligned} \text{Model A)} \quad F(s) &= \frac{M^2}{M^2 - s + \frac{1}{\pi} \Gamma \frac{s}{M} \ln \frac{-s}{M^2}}, \\ \text{Model B)} \quad F(s) &= \frac{M\Gamma}{M^2 - s + \frac{1}{\pi} M\Gamma \ln \frac{-s}{M^2}}, \end{aligned}$$

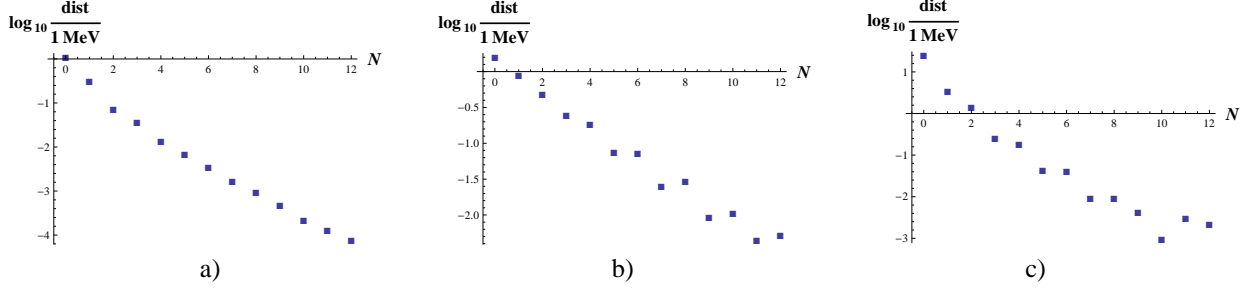


Figure 7: a), b) and c): respectively, the convergence of the  $P_1^N$  poles to the “physical” value in the models A, B and C. The distance from the fitted pole to the “physical” one is described by  $dist \equiv [(M^{\text{fit}} - M_p)^2 + (\Gamma^{\text{fit}} - \Gamma_p)^2]^{\frac{1}{2}}$ .

$$\text{Model C)} \quad F(s) = \frac{s \ln \frac{-s}{M^2}}{(M - i\Gamma/2)^2 - s}, \quad (26)$$

with  $M$  and  $\Gamma$  conveniently tuned in each case to produce the pole at  $s = s_p$ .

In order to simulate the physical situation we take the model (A for instance) and generate a series of “data” points with zero error, which would represent an ideal experimental situation where all the uncertainty would be theoretical. We fit the “data” for the modulus and phase-shift of  $F(s)$  and extract the optimal complex parameters  $a_k$  for each  $P_1^N$  Padé. Notice that this does not mean to fit  $|F(s)|$  (or the VFF phase) with a  $P_1^N$  Padé. The modulus and phase-shift of the data are, respectively, fitted with the modulus and phase-shift of  $P_1^N$ . The Padé pole  $s^{\text{fit}} = (M^{\text{fit}} - i\Gamma^{\text{fit}}/2)^2$  is found to converge to the “physical”  $s_p = (M_p - i\Gamma_p/2)^2$  of the model when  $N \rightarrow \infty$ . The approaching of the complex Padé pole to its limit value can be observed in Fig. 7. It is clear that the rate of converge depends on the kind of model, being faster for model A and slower for B and C.

#### 4.2. Application to experimental data

We proceed now to analyze the final compilation of ALEPH  $\pi\pi$  vector form-factor data for the squared modulus  $|F_{\pi\pi}(q^2)|^2$  [28] and the  $I = J = 1$   $\pi\pi$  scattering phase-shift  $\delta_{\pi\pi}$ , identical to the  $\pi\pi$  vector form-factor phase-shift in the

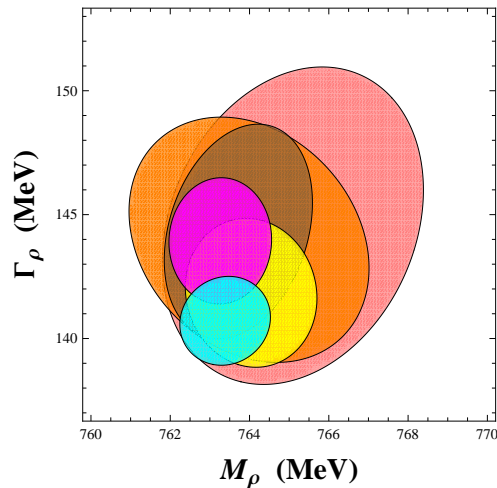


Figure 8: 68% CL regions for the rho pole mass and width from the different  $P_1^N$  fits. The smallest (cyan) ellipse provides the prediction for  $N = 3$  and the following growing orders in  $N$  are given by the ovals with larger and larger size.

elastic region  $4m_\pi^2 < q^2 < 4m_K^2$  (if multipion channels are neglected). This will be the range of application of  $P_1^N$  Padé analysis. For  $N \geq 3$  the fit  $\chi^2$  already lies within the 68% confidence level (CL) and becomes statistically acceptable. Their corresponding 68% CL regions for the pole mass and width predictions are shown in Fig. 8. The regions from the different fits overlap each other in a compatible way. The allowed ranges become larger and larger as  $N$  grows and the fit contains more and more free parameters.

At this point one needs to reach a compromise. On one hand the experimental (fit) errors have an statistical origin and increase as one considers higher order Padés  $P_1^N$ , with a larger number of parameters. On the other, the systematic theoretical (Padé) error decreases as  $N$  increases and the Padé converges to the actual VFF. In the present work we have taken  $N = 6$  as our best estimate as the new parameters of Padés with  $N \geq 7$  turn out to be all compatible with zero, introducing no information with respect to  $P_1^6$ . Furthermore, the different models studied before show that in any case the theoretical errors for mass and width result smaller than  $10^{-1}$ – $10^{-2}$  MeV for  $N \geq 6$ , being negligible compared to the  $O(1 \text{ MeV})$  experimental errors. This yields the determinations

$$M_\rho = 763.7 \pm 1.2 \text{ MeV}, \quad \Gamma_\rho = 144 \pm 3 \text{ MeV}, \quad (27)$$

which is found in reasonable agreement with former determinations obtained from more elaborated procedures and with similar size for the uncertainties:

[Ananthanarayan <i>et al.</i> [29] ]	$M_\rho = 762.5 \pm 2 \text{ MeV},$	$\Gamma_\rho = 142 \pm 7 \text{ MeV},$
[IAM [30] ]	$M_\rho = 754 \pm 18 \text{ MeV},$	$\Gamma_\rho = 148 \pm 20 \text{ MeV},$
[Zhou <i>et al.</i> [31] ]	$M_\rho = 763.0 \pm 0.2 \text{ MeV},$	$\Gamma_\rho = 139.0 \pm 0.5 \text{ MeV},$
[Pich and SC [8] ]	$M_\rho = 764.1 \pm 2.7_{-2.5}^{+4.0} \text{ MeV},$	$\Gamma_\rho = 148.2 \pm 1.9_{-5.9}^{+1.7} \text{ MeV}.$

(28)

## 5. Conclusions

The Padé approximants are important tools for the analysis of QCD amplitudes. They provide alternative determinations with competitive precision.

At low energies, we have been able to determine the first derivatives of the  $\pi\pi$ -VFF at the origin, this is, its quadratic charge radius  $\langle r^2 \rangle_V^\pi (= 6a_1)$  and the curvature  $c_V^\pi (= a_2)$ . For this, we used Euclidian data, i.e., from  $q^2 < 0$ .

Likewise, we were able to employ the Padé approximants to extract information about the hadronic resonance poles (the  $\rho(770)$  mass and width). The experimental Minkowskian VFF and  $\pi\pi$ -scattering data were analyzed by means of  $P_1^N$  Padés centered between the first and second production thresholds. We obtained the determinations  $M_\rho = 763.7 \pm 1.2 \text{ MeV}$  and  $\Gamma_\rho = 144 \pm 3 \text{ MeV}$ , with a competitive precision compared to other more elaborated and complex methods, in spite of the simplicity of the proposed procedure.

This study shows the Padé approximants, once again, as a useful tool for the investigation of QCD phenomenology. They provide alternative determinations and, in spite of their simplicity, they have been proven as an efficient and systematic instrument. Nevertheless, when no theorem supports the convergence of the Padé sequence, the extracted parameters may have little to do with the physical ones, as we saw in our LSM study of “Padé”-unitarizations in Sec. 3.

## References

- [1] P. Masjuan, S. Peris and J.J. Sanz-Cillero, Phys. Rev. D **78** (2008) 074028 [arXiv:0807.4893 [hep-ph]].
- [2] A. Dobado, M.J. Herrero and T.N. Truong, Phys. Lett. B **235** (1990) 134;  
T. Hannah, Phys. Rev. D **52** (1995) 4971-4975;  
A. Dobado and J.R. Pelaez, Phys. Rev. D **47** (1993) 4883-4888 [arXiv:hep-ph/9301276].
- [3] A. Dobado and J.R. Pelaez, Phys. Rev. D **56** (1997) 3057-3073 [arXiv:hep-ph/9604416].
- [4] P. Masjuan, J.J. Sanz-Cillero and J. Virto, Phys. Lett. B **668** (2008) 14-19 [arXiv:0805.3291 [hep-ph]].
- [5] J.R. Peláez, private communications.
- [6] W. M. Yao *et al.* [Particle Data Group], J. Phys. G **33** (2006) 1.
- [7] F. Guerrero and A. Pich, Phys. Lett. B **412** (1997) 382-388 [arXiv:hep-ph/9707347];  
D. Gomez Dumm, A. Pich and J. Portoles, Phys. Rev. D **62** (2000) 054014 [arXiv:hep-ph/0003320].

- [8] J. J. Sanz-Cillero and A. Pich, Eur. Phys. J. C **27** (2003) 587 [arXiv:hep-ph/0208199].
- [9] A. Pich and J. Portolés, Phys. Rev. D **63** (2001) 093005 [arXiv:hep-ph/0101194].
- [10] S.R. Amendolia *et al.* (NA7 Collaboration), Nucl. Phys. B **277** (1986) 168.
- [11] V. Tadevosyan *et al.* (JLab F(pi) Collaboration), Phys. Rev. C **75** (2007) 055205 [arXiv:nucl-ex/0607007].
- [12] T. Horn *et al.* (JLab F(pi)-2 Collaboration), Phys. Rev. Lett. **97** (2006) 192001 [arXiv:nucl-ex/0607005];  
T. Horn *et al.* (JLab) [arXiv:0707.1794 [nucl-ex]].
- [13] C. N. Brown *et al.*, Phys. Rev. D **8** (1973) 92;  
C. J. Bebek *et al.*, Phys. Rev. D **9** (1974) 1229.  
C. J. Bebek *et al.*, Phys. Rev. D **13** (1976) 25.  
We take as input the reanalysis of these results and the final compilation performed in C. J. Bebek *et al.*, Phys. Rev. D **17** (1978) 1693.
- [14] P. Brauel *et al.*, Z. Phys. C3, 101 (1979). For our input we took the reanalysis of these data performed in Ref. [11].
- [15] Dally *et al.*, Phys. Rev. Lett. **39** (1977) 1176.
- [16] G. P. Lepage and S. J. Brodsky, Phys. Lett. B **87** (1979) 359; Phys. Rev. D **22** (1980) 2157; Phys. Rev. D **24** (1981) 2903.
- [17] H. Leutwyler, [arXiv:hep-ph/0212324];  
G. Colangelo, Nucl. Phys. Proc. Suppl. **131** (2004) 185-191 [arXiv:hep-ph/0312017].
- [18] G. Colangelo, J. Gasser and H. Leutwyler, Nucl. Phys. B **603** (2001) 125 [arXiv:hep-ph/0103088].
- [19] J.F. de Troconiz and F.J. Yndurain, Phys. Rev. D **65** (2002) 093001 [arXiv:hep-ph/0106025]; Phys. Rev. D **71** (2005) 073008 [arXiv:hep-ph/0402285].
- [20] J. Bijnens, G. Colangelo and P. Talavera, JHEP **05** (1998) 014 [arXiv:hep-ph/9805389].
- [21] P. A. Boyle *et al.*, [arXiv:0804.3971 [hep-lat]].
- [22] G.Y. Qin, W.Z. Deng, Z.G. Xiao and H.Q. Zheng, Phys. Lett. B **542** (2002) 89-99 [arXiv:hep-ph/0205214].
- [23] J.R. Pelaez, Phys. Rev. Lett. **92** (2004) 102001 [arXiv:hep-ph/0309292];  
J.R. Pelaez and G. Rios, Phys. Rev. Lett. **97** (2006) 242002 [arXiv:hep-ph/0610397].
- [24] T. Hannah, Phys. Rev. D **55** (1997) 5613-5626 [arXiv:hep-ph/9701389].
- [25] J. Gasser and H. Leutwyler, Annals Phys. **158** (1984) 142.
- [26] R. de Montessus de Ballore, Bull. Soc. Math. France **30** (1902), 28-36.
- [27] G.A. Baker and P. Graves-Morris, *Padé Approximants, encyclopedia of mathematics and its applications*, Cambridge Univ. Press. 1996.
- [28] S. Schael *et al.* (ALEPH Coll), Phys. Rept. **421** (2005) 191-284 [arXiv:hep-ex/0506072];  
M. Davier, A. Hocker and Z. Zhang, Rev. Mod. Phys. **78** (2006) 1043-1109 [arXiv:hep-ph/0507078].
- [29] B. Ananthanarayan, G. Colangelo, J. Gasser and H. Leutwyler, Phys. Rept. **353** (2001) 207-279 [arXiv:hep-ph/0005297].
- [30] J.R. Pelaez and A. Gómez-Nicola, *Gargnano 2002, Quark confinement and the hadron spectrum* 349-351 [arXiv:hep-ph/0212042];  
J.R. Pelaez, Mod. Phys. Lett. A **19** (2004) 2879-2894 [arXiv:hep-ph/0411107].
- [31] Z.Y. Zhou, G.Y. Qin, P. Zhang, Z.G. Xiao and H.Q. Zheng, JHEP **0502** (2005) 043 [arXiv:hep-ph/0406271].